Simulations of nonhelical hydromagnetic turbulence

Nils Erland L. Haugen[*]

Department of Physics, The Norwegian University of Science and Technology, Høyskoleringen 5, N-7034 Trondheim, Norway

Axel Brandenburg[†]

NORDITA, Blegdamsvej 17, DK-2100 Copenhagen Ø, Denmark

Wolfgang Dobler[‡]

Kiepenheuer-Institut für Sonnenphysik, Schöneckstraße 6, D-79104 Freiburg, Germany

Nonhelical hydromagnetic forced turbulence is investigated using large scale simulations on up to 256 processors and 1024^3 mesh points. The magnetic Prandtl number is varied between 1/8 and 30, although in most cases it is unity. When the magnetic Reynolds number is based on the inverse forcing wave number, the critical value for dynamo action is shown to be around 35 for magnetic Prandtl number of unity. For small magnetic Prandtl numbers we find the critical magnetic Reynolds number to increase with decreasing magnetic Prandtl number. The Kazantsev $k^{3/2}$ spectrum for magnetic energy is confirmed for the kinematic regime, i.e., when nonlinear effects are still unimportant and when the magnetic Prandtl number is unity. In the nonlinear regime, the energy budget converges for large Reynolds numbers (around 1000) such that for our parameters about 70% is in kinetic energy and about 30% is in magnetic energy. The energy dissipation rates are converged to 30% viscous dissipation and 70% resistive dissipation. Second-order structure functions of the Elsasser variables give evidence for a $k^{-5/3}$ spectrum. Nevertheless, the three-dimensional spectrum is close to $k^{-3/2}$, but we argue that this is due to the bottleneck effect. The bottleneck effect is shown to be equally strong both for magnetic and nonmagnetic turbulence, but it is far weaker in one-dimensional spectra that are normally studied in laboratory turbulence. Structure function exponents for other orders are well described by the She-Leveque formula, but the velocity field is significantly less intermittent and the magnetic field is more intermittent than the Elsasser variables.

I. INTRODUCTION

Dynamo action, i.e., the conversion of kinetic energy into magnetic energy, plays an important role in astrophysical bodies ranging from stars to galaxies and even clusters of galaxies. The gas in these bodies is turbulent and the magnetic Reynolds numbers are huge (10^{10} to 10^{20}). This suggests that there should be dynamo action and that the magnetic fields should be amplified on the time scale of the turbulent turnover time [1,2]. The magnetic fields of many astrophysical bodies show a great deal of spatiotemporal order (e.g., an 11-year cycle and equatorward migration of the magnetic field in the case of the sun), which can basically be explained by the helicity effect [3–5]. In many other astrophysical environments, however, the helicity effect is probably completely irrelevant (e.g., in the solar wind [6], clusters of galaxies [7], and the early universe after recombination [8]). In all these cases the magnetic field does not show spatiotemporal order of the type known for helical hydromagnetic turbulence [5]. Both analytic theory [9] as well as simulations [10] have long shown that dynamo action is possible even without kinetic helicity, but that the field is

then spatially highly intermittent with substantial power at small length scales. Hydromagnetic turbulence has recently also been studied in the laboratory [11–13], but there the magnetic Reynolds numbers are still rather small. Therefore, numerical simulations are currently the most powerful tool.

In spite of significant progress over the past two decades, the form of the energy spectrum at large magnetic Reynolds numbers is still a matter of debate. Particular progress has been made in the case where there is a large scale field. Goldreich and Sridhar [14] have proposed that the magnetic energy spectrum has a $k^{-5/3}$ inertial range due to the anisotropy imposed by the local magnetic field. This was in conflict with the earlier Iroshnikov-Kraichnan [15] $k^{-3/2}$ spectrum, which assumes isotropy, but can now be ruled out [16–18]. Some simulations still show a $k^{-3/2}$ spectrum, but this is probably due to the bottleneck effect; see below. A $k^{-5/3}$ total energy spectrum has, however, clearly been seen in decaying hydromagnetic turbulence [17]. Here the total energy spectrum is simply the sum of kinetic and magnetic energy spectra.

The case of an imposed large scale magnetic field with approximate equipartition strength is in some respects similar to the case of a self-generated large scale field which emerges if there is helicity in the flow [4,10,19]. In the latter case of helical turbulence, and for unit magnetic Prandtl number, kinetic and magnetic energy spectra are in almost perfect equipartition on all scales smaller than the forcing scale (see Fig. 11 of Ref. [5]), and the two spectra tend to

[*]Electronic address: nils.haugen@phys.ntnu.no

[†]Electronic address: brandenb@nordita.dk

[‡]Electronic address: Wolfgang.Dobler@kis.uni-freiburg.de

TABLE I. Summary of earlier work on hydromagnetic turbulence simulations. In addition to the reference of each paper, we give for convenience a more descriptive abbreviation. In Ref. [18] the largest resolution was $N^3 = 256^2 \times 512$, so we have listed the geometrical mean corresponding to 322^3. The column "Hyper" indicates whether or not hyperviscosity or hyperdiffusivity have been used; "Artif" stands for shock-capturing artificial viscosity. In the column "Forced," the abbreviation "Hel" stands for helical, "Noh" for nonhelical, "Decay" for decaying turbulence without forcing, and "~Noh" means that there is some small fraction of helicity, but due to a small scale separation between the forcing and the box scale the simulation is practically nonhelical. In the column $\langle \boldsymbol{B} \rangle$, "Ext" indicates the use of an external field. The column "Compr" signifies whether the models are compressible.

Paper	Ref.	N	Hyper	Forced	$\langle \boldsymbol{B} \rangle$	Compr	Pr_M
MFP81	[10]	64	Both	Hel/noh	0	No	1
B01	[5]	120	No	Hel	0	Yes	0.1–100
KYM91	[23]	128	Yes	Hel	0	No	1
MMDM01	[29]	128	No	Decay	Ext/0	No	1
OMG98	[30]	128	No	Decay	Ext/0	Both	1
CL03	[31]	216		Decay	Ext	Yes	1
MLKB98	[32]	256	Artif	Decay	0	Yes	1
CV00	[16]	256	Both	~Noh	Ext	No	1
MC01	[25]	256	Both	Noh	Ext/0	No	1–2500
MG01	[18]	322	Yes	Noh	Ext	No	1
CLV02	[33]	384	Yes	~Noh	Ext	No	Large
BNP02	[34]	500	Yes	Noh	Ext	Yes	1
BM00	[17]	512	Both	Decay	0	No	1
HBD03	[35]	1024	No	Noh	0	Yes	1

approach a $k^{-5/3}$ inertial range as the magnetic Reynolds number is increased. In the former case, equipartition throughout the inertial range may require that the energy of the imposed field is comparable to the kinetic energy; for stronger fields the magnetic energy becomes suppressed at small scales [20]. If the magnetic Prandtl number is larger than unity, the resistive cutoff is prolonged to larger wave numbers by a k^{-1} spectrum [21]. Nevertheless, some authors have suggested that even in the nonlinear regime the spectral magnetic energy increases toward smaller scales, similar to the kinematic regime where the energy spectrum scales as $k^{+3/2}$ [9,22].

In the absence of an imposed large scale magnetic field, and with no helicity, the situation is in many ways different. Early simulations suggest that the magnetic field is dominated by small scale power [10]. Even for a magnetic Prandtl number of unity the magnetic energy exceeds the kinetic energy at small scales [23–25], a result that is otherwise (with imposed field or with helicity) only obtained for magnetic Prandtl numbers larger than unity [5,21,25,26].

The main problem in determining the energy spectrum at large hydrodynamic and magnetic Reynolds numbers is the lack of a proper inertial range in the magnetic field. Another problem is that in the absence of helicity the dynamo is much weaker and one needs significantly (about 20×) larger magnetic Reynolds numbers before the dynamo is even excited. In practice, this means that a resolution of 128^3 or more is mandatory.

The shortness or even lack of an inertial range has frequently led to the use of hyperviscosity and hyperdiffusivity [10,23], which has the tendency to extend the inertial range

and to shorten the dissipative subrange. However, in recent years it has become clear that these modifications to the viscosity and diffusion operators can affect major parts of the inertial subrange and make it shallower. This is also referred to as the bottleneck effect which is present already for ordinary viscosity [27], but it becomes greatly exaggerated with hyperviscosity; compare Figs. 8 and 11 of Ref. [17]. In helical dynamos the saturation time becomes significantly prolonged and the final saturation level is artificially enhanced [28]. It is therefore important to use simulations with regular viscosity and magnetic diffusivity at high enough resolution.

A lot of work has already been done in order to determine the form of the magnetic energy spectrum at large magnetic Reynolds numbers. Some of the relevant papers are listed in Table I, where we indicate the main properties of their setups. In addition to the papers mentioned above, we have included a number of additional ones [29–35], some of which will be discussed below in more detail.

In a recent paper, we already presented some initial results on energy spectra at a resolution of up to 1024^3 mesh points; see Ref. [35], hereafter referred to as Paper I. In the present paper we discuss the associated results for the critical magnetic Reynolds number for dynamo action, we consider a range of different values of the magnetic Prandtl number, compare with the case of finite magnetic helicity, and present visualizations of the magnetic field and the dissipative structures in hydromagnetic turbulence. We look in detail at the energy spectra and the structure functions of total, kinetic, and magnetic energies. The simulations have been carried out using the Pencil Code [36] which is a memory-efficient high-order finite difference code using the 2N-RK3 scheme

TABLE II. Summary of runs with $Pr_M = 1$ (thus $Re = Re_M$) and forcing at $k_f = 1.5$. In all cases, except D2, we have $u_{rms} \approx 0.12$. Run D2 had a stronger forcing, and therefore $u_{rms} \approx 0.18$. The Taylor microscale Reynolds number is $Re_\lambda = u_{1D} \ell_\lambda / \nu$, where $u_{1D} = u_{rms}/\sqrt{3}$ is the rms velocity in one direction and $\ell_\lambda = \sqrt{5} u_{rms} / \omega_{rms}$ is the Taylor microscale, where ω_{rms} is the rms vorticity.

Run	Resolution	$\nu \times 10^4$	Re_λ	Re_M	B_{rms}	$\epsilon_K \times 10^4$	$\epsilon_M \times 10^4$
A	64^3	7.0	80	120	0.052	1.0	1.2
B	128^3	4.0	110	190	0.060	0.79	1.4
C	256^3	2.0	160	420	0.062	0.78	1.6
D	512^3	1.5	190	540	0.072	0.68	1.7
D2	512^3	2.0	180	600	0.092	2.2	5.0
E	1024^3	0.8	230	960	0.075	0.63	1.5

of Williamson [37]. Our approach is technically similar to that used in Ref. [5]. The Pencil Code is fully compressible; we therefore consider the weakly compressible case (the Mach number is around 0.1), which can be considered as an approximation to the incompressible case. A list of parameters for most runs discussed in the present paper is given in Table II.

II. EQUATIONS

We adopt an isothermal equation of state with constant (isothermal) sound speed c_s, so the pressure p is related to the density ρ by $p = \rho c_s^2$. The equation of motion is written in the form

$$\frac{D\boldsymbol{u}}{Dt} = -c_s^2 \boldsymbol{\nabla} \ln \rho + \frac{\boldsymbol{J} \times \boldsymbol{B}}{\rho} + \boldsymbol{F}_{visc} + \boldsymbol{f}, \tag{1}$$

where $D/Dt = \partial/\partial t + \boldsymbol{u} \cdot \boldsymbol{\nabla}$ is the advective derivative, $\boldsymbol{J} = \boldsymbol{\nabla} \times \boldsymbol{B}/\mu_0$ is the current density, μ_0 is the vacuum permeability,

$$\boldsymbol{F}_{visc} = \nu \left(\nabla^2 \boldsymbol{u} + \tfrac{1}{3} \boldsymbol{\nabla} \boldsymbol{\nabla} \cdot u + 2\mathbf{S} \cdot \boldsymbol{\nabla} \ln \rho \right) \tag{2}$$

is the viscous force, $\nu = const$ is the kinematic viscosity,

$$\mathbf{S}_{ij} = \frac{1}{2} \left(\frac{\partial u_i}{\partial x_j} + \frac{\partial u_j}{\partial x_i} - \frac{2}{3} \delta_{ij} \boldsymbol{\nabla} \cdot \mathbf{u} \right) \tag{3}$$

is the traceless rate of strain tensor, and $\boldsymbol{f}$ is a random forcing function that consists of nonhelical plane waves (see below). The continuity equation is written in terms of the logarithmic density,

$$\frac{D \ln \rho}{Dt} = -\boldsymbol{\nabla} \cdot \mathbf{u}, \tag{4}$$

and the induction equation is solved in terms of the magnetic vector potential $\mathbf{A}$, with $\mathbf{B} = \boldsymbol{\nabla} \times \mathbf{A}$, so

$$\frac{\partial \mathbf{A}}{\partial t} = \mathbf{u} \times \mathbf{B} + \eta \nabla^2 \mathbf{A}, \tag{5}$$

where $\eta = const$ is the magnetic diffusivity.

We use periodic boundary conditions in all three directions for all variables. This implies that the mass in the box is conserved, i.e., $\langle \rho \rangle = \rho_0$, where ρ_0 is the value of the initially uniform density, and angular brackets denote volume averages. We adopt a forcing function $\boldsymbol{f}$ of the form

$$\boldsymbol{f}(\boldsymbol{x},t) = \mathrm{Re}\{N\boldsymbol{f}_{\boldsymbol{k}(t)} \exp[i\boldsymbol{k}(t) \cdot \boldsymbol{x} + i\phi(t)]\}, \tag{6}$$

where $\boldsymbol{x}$ is the position vector. The wave vector $\boldsymbol{k}(t)$ and the random phase $-\pi < \phi(t) \leq \pi$ change at every time step, so $\boldsymbol{f}(\boldsymbol{x},t)$ is δ correlated in time. For the time-integrated forcing function to be independent of the length of the time step δt, the normalization factor N has to be proportional to $\delta t^{-1/2}$. On dimensional grounds it is chosen to be $N = f_0 c_s (|\boldsymbol{k}| c_s / \delta t)^{1/2}$, where f_0 is a nondimensional forcing amplitude. The value of the coefficient f_0 is chosen such that the maximum Mach number stays below about 0.5; in practice, this means $f_0 = 0.02, \ldots, 0.05$.

At each time step we select randomly one of many possible wave vectors in a certain range around a given forcing wave number. The average wave number is referred to as k_f. We force the system with nonhelical transversal waves,

$$\boldsymbol{f}_{\boldsymbol{k}} = (\boldsymbol{k} \times \boldsymbol{e})/\sqrt{\boldsymbol{k}^2 - (\boldsymbol{k} \cdot \boldsymbol{e})^2}, \tag{7}$$

where $\boldsymbol{e}$ is an arbitrary unit vector not aligned with $\boldsymbol{k}$; note that $|\boldsymbol{f}_{\boldsymbol{k}}|^2 = 1$.

The resulting flows are characterized by the kinetic and magnetic Reynolds numbers,

$$\mathrm{Re} = \frac{u_{rms}}{\nu k_f}, \quad \mathrm{Re}_M = \frac{u_{rms}}{\eta k_f}, \tag{8}$$

respectively. Their ratio is the magnetic Prandtl number,

$$Pr_M = \nu/\eta = \mathrm{Re}_M/\mathrm{Re}, \tag{9}$$

which is unity for most of the runs.

We use nondimensional quantities by measuring length in units of $1/k_1$ (where $k_1 = 2\pi/L$ is the smallest wave number in the box of size L), speed in units of the isothermal sound speed c_s, density in units of the initial value ρ_0, and magnetic field in units of $(\mu_0 \rho_0 c_s^2)^{1/2}$.

III. THE KINEMATIC PHASE AND APPROACH TO SATURATION

As initial condition we use a weak random seed magnetic field. In this section we consider the time interval during which the amplitude of the magnetic energy spectrum grows
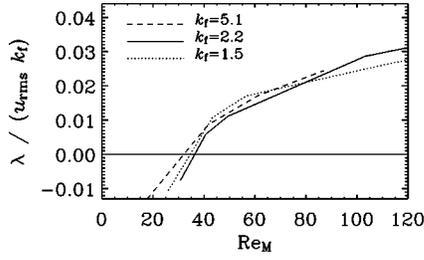
FIG. 1. Growth rate vs Re_M for different values of k_f, and for $Pr_M=1$. The curves represent linear fits through the data. Note that the critical value is around 35 for all the different runs. The resolution varies between 64^3 and 256^3, and $f_0=0.05$ in all runs, resulting in $u_{rms} \approx 0.2$.

exponentially and is still small compared to the kinetic energy spectrum for all wave numbers.

A. Critical magnetic Reynolds number

We have determined the growth rate of the rms magnetic field, $\lambda \equiv d \ln B_{rms}/dt$, for different values of Re_M and Pr_M. Interpolating the curves $\lambda = \lambda(Re_M)$ through zero, we find the critical value, $Re_M^{(crit)}$, which is roughly independent of k_f; see Fig. 1. For the case $Pr_M=1$ we find $Re_M^{(crit)} \approx 35$, which is consistent with the value obtained using a modified version of the eddy-damped quasinormal Markovian (EDQNM) approximation [38] which gives $Re_M^{(crit)}=29$.

As the value of Pr_M is lowered, the critical magnetic Reynolds number increases slowly like

$$Re_M^{(crit)} \approx 35 \, Pr_M^{-1/2}, \qquad (10)$$

see Fig. 2. It remains uncertain whether this scaling persists to very small values of Pr_M that are relevant to liquid metal experiments or to stellar convection zones. We note, however, that the EDQNM approximation predicts [38] that the critical magnetic Reynolds number is independent of Pr_M for a large range of Re and Pr_M. Based on application of the Kazantsev model Schekochihin *et al.* [39] have shown that, if the correlation time is assumed to be independent of wave number, there exists a finite value of Pr_M below which dynamo action is impossible. On the other hand, if the correlation time is proportional to the eddy turnover time, $\sim k^{-2/3}$, dynamo action should be possible even for very small values of Pr_M.
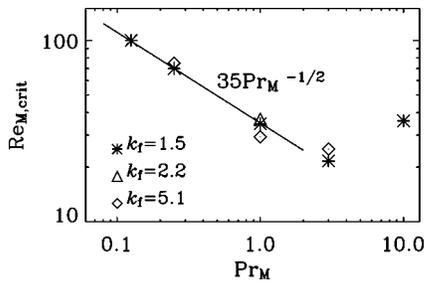
FIG. 2. Critical magnetic Reynolds number as a function of magnetic Prandtl number for runs with different forcing scale.
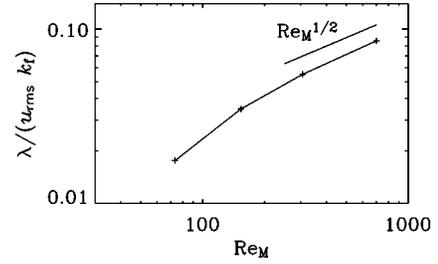
FIG. 3. Log-log plot of growth rate vs Re_M for $k_f=1.5$, and $Pr_M=1$. The curves represent linear fits through the data. Note that there seems to be an $Re_M^{1/2}$ dependence on λ as Re_M is increased. The resolution varies between 128^3 and 512^3.

For larger magnetic Reynolds numbers the growth rate of the magnetic field seems to approach a $Re_M^{1/2}$ dependence; see Fig. 3. Such a power law would be expected if the growth rate is proportional to the eddy turnover time at the dissipation wave number, k_d, i.e., $\lambda \propto k_d^{2/3} \propto Re_M^{1/2}$, where we have used $Re_M \propto k_d^{4/3}$ [40]. We must emphasize, however, that the Re_M scaling is as yet rather short.

B. The Kazantsev spectrum

Under the somewhat unrealistic assumption that the velocity field is δ correlated in time, one can, for a given spatial correlation function of the velocity, and ignoring magnetic feedback, derive an evolution equation for the correlation function of the magnetic field [9,41] (see Ref. [42] for a nonlinear extension). This can be rewritten as an integro-differential equation in k space which, in turn, can be written as a diffusion equation in k space if the velocity field has only power at large scales [9,22]. The result is $E_k^M(k) \propto k^{3/2} K_{n(\lambda)}(k/k_\eta)$, where K_n is the Macdonald function (modified Bessel function of the third kind), $\lambda \approx 3/4$ is an eigenvalue, and $n(\lambda) \approx 0$; see Ref. [43] for details. In linear theory the amplitude of the solution is, however, undetermined and grows exponentially if the magnetic Reynolds number exceeds a critical value of about 30–60 [41].

In comparison with our simulations we see qualitative agreement as far as the $k^{3/2}$ slope is concerned. As long as the magnetic field is weak, the velocity field has an energy spectrum with the expected $k^{-5/3}$ Kolmogorov scaling; see Fig. 4. During this phase the spectral magnetic energy grows at all
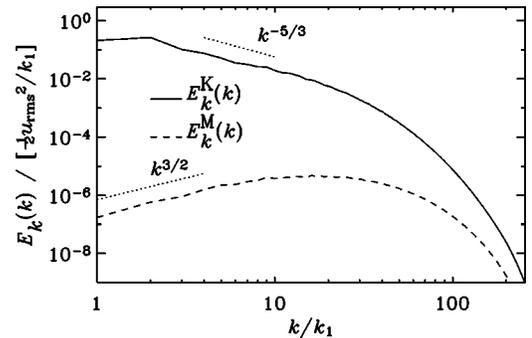
FIG. 4. Early spectra of kinetic and magnetic energy, normalized by $\frac{1}{2}u_{rms}^2/k_1$, during the kinematic stage of run D2.
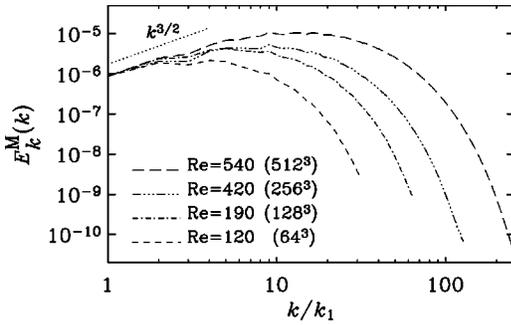
FIG. 5. Convergence of the magnetic power spectrum toward the $k^{3/2}$ scaling as Re_M increases. All spectra correspond to the kinematic stages of runs A–D with $Pr_M = 1$, but have been rescaled to make them overlap at small values of k. The dimension on the ordinate is therefore arbitrary.

wave numbers exponentially in time and the spectrum has the expected $k^{3/2}$ Kazantsev [9] slope; see Fig. 4. The convergence toward Kazantsev scaling is seen in Fig. 5, where we have plotted the magnetic energy spectrum for runs with Re_M between 120 and 540. (The kinematic growth phase for run E was not available, because we restarted run E from run D after it had already reached saturation.)

Originally, Kazantsev obtained the $k^{3/2}$ spectrum under the assumption that the velocity has power only at large scales, which would correspond to a large value of Pr_M. Simulations for large Pr_M have indeed confirmed the Kazantsev slope [25]. Our results now show that the Kazantsev spectrum is also obtained for $Pr_M = 1$.

The values of $\eta (= \nu)$ and Re_M used for the different runs discussed above are summarized in Table II.

C. Approach to saturation

One would naively expect that the onset of saturation happens rapidly on a dynamical time scale. That this is not the case in helical hydromagnetic turbulence came originally as a surprise, but it is now well understood to be a consequence of asymptotic magnetic helicity conservation. The same argument does not apply to nonhelical turbulence. Nevertheless, there may still be a slowdown in the saturation behavior at small wave numbers [43].

The clarification of this question is hampered by the fact that one needs very high resolution before one can with certainty distinguish resistive time scales from dynamical ones. Figure 6 shows the saturation behavior for two different values of k in a run with 512^3 meshpoints. The initial growth is clearly exponential both at $k=1$ and at $k=16$. However, when the magnetic energy at $k=16$ saturates at $t \approx 100/(u_{rms}k_f)$, the magnetic energy at $k=1$ seems to continue growing approximately linearly [43]; see Fig. 6 for $100 < u_{rms}k_f t < 200$. Looking at the simulation at later times one sees, however, that the time sequence is actually very bursty and that the approximately linear growth in the interval $100 < u_{rms}k_f t < 200$ was only a transient. (This is best seen in the inset of Fig. 6 where the energies are shown in a linear plot.) We can therefore not confirm with certainty that the difference in the saturation
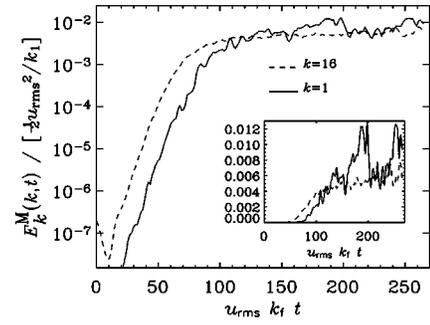
FIG. 6. Saturation behavior of the spectral magnetic energy at wave numbers $k=1$ (solid line) and $k=16$ (dashed line) for run D2. Note the slow saturation behavior for $k=1$.

times for $k=1$ and $k=16$ is explained by the difference between dynamical and resistive time scales.

In the following section we present further properties of these runs after the time when the field has reached saturation.

IV. DYNAMICALLY SATURATED PHASE

When the magnetic energy has reached a certain fraction of the kinetic energy, the magnetic field stops growing exponentially and eventually reaches a statistically steady state. In this section we discuss the properties of this state.

A. Energy spectra

As saturation sets in, the spectral magnetic energy begins to exceed the spectral kinetic energy at small scales; see the upper panel of Fig. 7, where we also show the total energy spectrum, $E_k^T = E_k^K + E_k^M$. There is a short inertial range with an approximate Kolmogorov $k^{-5/3}$ spectrum, but, as already reported in Paper I and discussed in Ref. [44], there is a strong bottleneck effect in the three-dimensional spectra which is less strong in one-dimensional spectra. Therefore, we plot in Fig. 7 for comparison both three-dimensional and one-dimensional spectra for the same run E. With one-dimensional spectra we mean spectra calculated from variations along one of the coordinate directions only. Throughout this paper, we refer to the one-dimensional spectra as the sum of the longitudinal plus two times the transversal spectra [44]. To obtain the three-dimensional spectra we have integrated over three-dimensional shells in $\boldsymbol{k}$ space, assuming isotropy.

Much of the large-scale kinetic energy is probably transferred directly to smaller-scale magnetic fields. At large scales the three-dimensional magnetic energy spectrum is weakly increasing, it peaks at $k=5$, and then joins the $k^{-5/3}$ slope of kinetic energy, but with a ~ 2.5 times larger amplitude. The one-dimensional energy spectrum, on the other hand, is monotonically decreasing also for small wave numbers.

All spectra terminate around the nominal dissipation cutoff wave number, $k_d = (\epsilon/\nu^3)^{1/4}$, where $\nu = \eta$ and $\epsilon = \epsilon_K + \epsilon_M$ is the total energy dissipation rate per unit mass, and
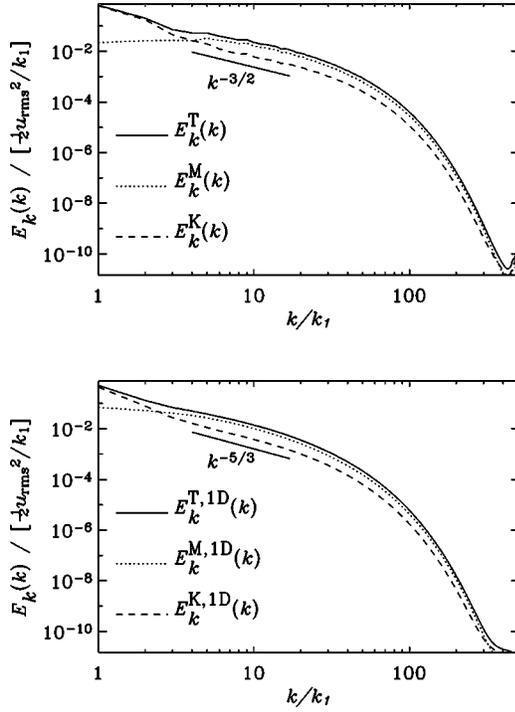
FIG. 7. Three-dimensional (upper panel) and one-dimensional (lower panel) time averaged spectra, normalized by $\frac{1}{2}u_{rms}^2/k_1$, for run E with a resolution of 1024^3 mesh points. The energy spectra have been averaged over a period of five turnover times $(u_{rms}k_f)^{-1}$.

$$\epsilon_K = 2\nu\langle\rho\mathbf{S}^2\rangle/\rho_0 \quad \text{and} \quad \epsilon_M = \eta\mu_0\langle\mathbf{J}^2\rangle/\rho_0 \qquad (11)$$

are the contributions from viscous and Ohmic dissipation, respectively. As the resolution is increased, the inertial range of the total energy spectrum becomes progressively longer (see Paper I). For run E we find $k_d \approx 142$. The "hook" in the spectrum for $k > 400$ (see Fig. 7) is probably a consequence of finite resolution and is typical also of turbulence simulations using spectral codes [45].

For the numerical simulations to work and to reproduce the turbulent cascade reliably, a certain minimum dynamic range in the compensated spectrum $k^{5/3}E_k(k)$ is necessary. We emphasize that this dynamic range increases with increasing Reynolds number, as can be seen in Fig. 8, where we have used viscosities close to the minimum values required for reliable results.

Looking at one-dimensional spectra of the magnetic, kinetic, and total energy (denoted by $E_k^{M,1D}$, $E_k^{K,1D}$, and $E_k^{T,1D}$), compensated with $\epsilon^{-2/3}k^{5/3}$, one sees that around $k=10$ there is a short range where all three compensated spectra are flat; see Fig. 9. We emphasize again that this is seen only in the higher-resolution runs.

There is some ambiguity as to what one calls the inertial range. Here we refer to inertial range as only the range where the *total* energy spectrum is compatible with a $k^{-5/3}$ slope. The kinetic energy alone, however, can show a $k^{-5/3}$ slope already for smaller wave numbers; see Fig. 8.

B. Comparison with nonmagnetic turbulence

For comparison we show the resulting spectra for purely hydrodynamic turbulence without magnetic fields and find
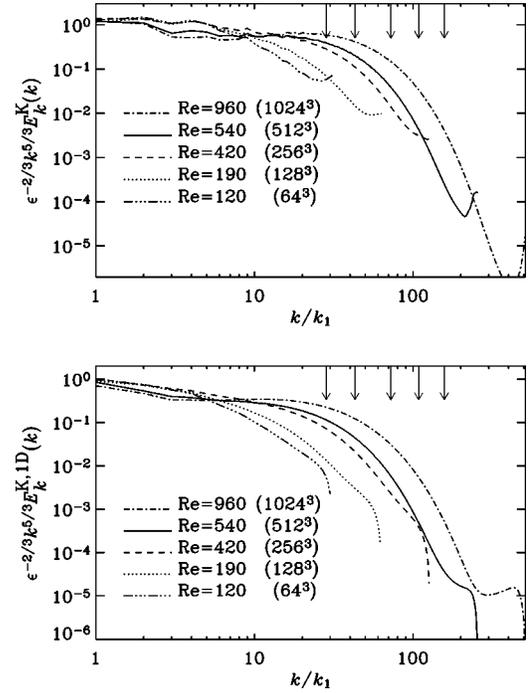
FIG. 8. Convergence of compensated three-dimensional (top) and one-dimensional (bottom) energy spectra of kinetic energy. The vertical arrows at the top show the dissipation cutoff wave number $(\epsilon/\nu^3)^{1/4}$ for the different resolutions.

again very similar bottleneck behavior, as shown in Fig. 10. A similar bottleneck effect is also found in other numerical simulations on up to 1024^3 mesh points [46,47]. As one increases the resolution even further (up to 4096^3 mesh points) [48], the bottleneck assumes an asymptotic shape, and begins to separate from the inertial range. A weak bottleneck effect is found even in wind tunnel experiments [49,50]. In such experiments one usually measures one-dimensional longitudinal energy spectra, and hence a much weaker bottleneck
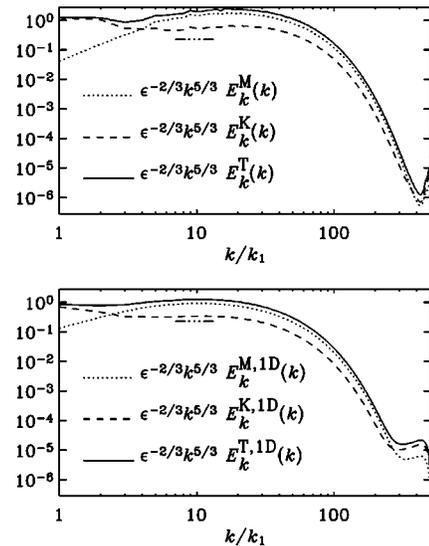
FIG. 9. Compensated magnetic, kinetic, and total three- and one-dimensional energy spectra for run E.
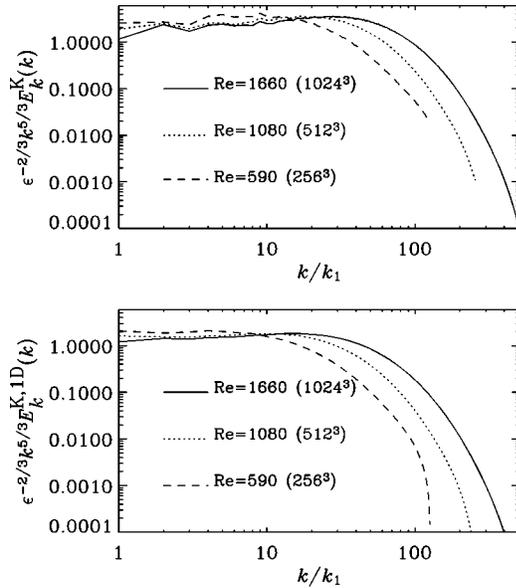
FIG. 10. Same as Fig. 8, but for a run without magnetic fields (pure hydrodynamics), for three different values of Re. Note the appearance of a bottleneck effect in the range $10 < k < 50$, particularly in the 3 D spectra. For these runs $k_f = 1.5$, and $u_{rms} \approx 0.18$.

effect is expected [44]. A physical explanation of the bottleneck effect is found in Ref. [27].

C. Subinertial range behavior

For the saturated state, Fig. 11 shows that for $k \lesssim 5$ the magnetic energy spectrum follows approximately a $k^{1/3}$ behavior, as was originally expected by Batchelor [1]. The same slope has also been found for convective turbulence at the time when the magnetic field is still weak [51], and, more recently (but probably for different reasons) for ABC-flow dynamos [52].

For wave numbers much less than the forcing wave number (subinertial range), the magnetic and kinetic energy spectra increase with k approximately like k^2. The theory for this spectrum is reviewed in the book by Lesieur [53]. This scaling is best seen in spectra where the turbulence is forced at
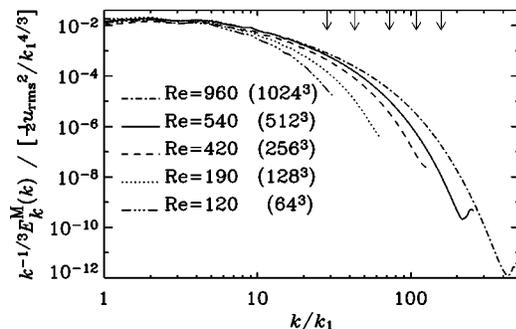
FIG. 11. Saturated three-dimensional magnetic energy spectra compensated by $k^{-1/3}$. The results are comparable with the vorticitylike $k^{1/3}$ scaling at small wave numbers ($k < 4$). The vertical arrows at the top show the dissipation cutoff wave number $(\epsilon/\nu^3)^{1/4}$ for the different resolutions.
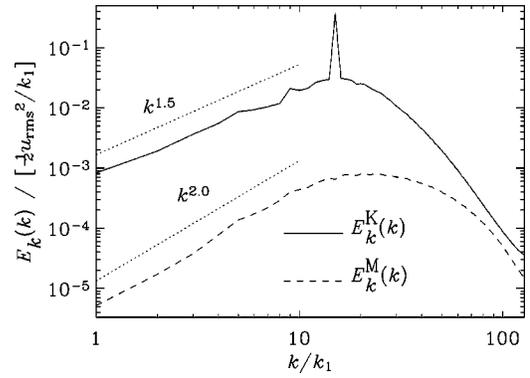
FIG. 12. The subinertial range of hydromagnetic turbulence forced at $k_f = 15$ and normalized by $\frac{1}{2} u_{rms}^2 / k_1$. $Re_M \approx 37$, 256^3 mesh points, $Pr_M = 1$.

$k_f \gg k_1 \equiv 1$; see Fig. 12 where $k_f = 15$. In this figure the kinetic spectrum is somewhat shallower and scales more like $k^{1.5}$. In this run, the magnetic energy is saturated, and yet it is only about 4% of the kinetic energy. This is mainly because the magnetic Reynolds number is only about 37, so the run is just weakly supercritical.

D. Reynolds number dependence

In Fig. 13 we show total energy spectra for three values of $Re = Re_M$ between 270 and 960. In the first case with $Re = Re_M = 270$ the compensated spectrum shows a reasonably flat range with a Kolmogorov constant $C_{KYM} \approx 1.3$, which is somewhat less than the value of 2.1 found by Kida *et al.* [23]. In the second case with $Re = Re_M = 440$ the compensated spectrum shows clear indications of excess power just before turning into the dissipative subrange. This is just the bottleneck effect and it becomes even more dramatic in the third case with $Re = Re_M = 960$. Thus, the bottleneck effect is only seen at sufficiently large resolution.

In order to assess the reliability of the results, we have carried out a convergence study using the same value of ν, but different mesh resolution; see the second panel of Fig. 13. In both cases, $\nu = \eta = 2 \times 10^{-4}$, while $u_{rms} = 0.13$ for 512^3 mesh points and 0.12 for 256^3. The energy dissipation is also similar, $\epsilon = 2.8 \times 10^{-4}$ for 512^3 mesh points and 2.3×10^{-4} for 256^3. The compensated energy spectra agree quite well for the two different resolutions, and both show excess power (bottleneck effect) just before turning into the dissipative subrange. This supports the conclusion that the excess power is not a numerical artifact.

E. Convergence of energy and dissipation rate

In the saturated state, the fractional magnetic and kinetic energies tend to a constant value at large Reynolds number, with

$$E_M : E_K \approx 0.3 : 0.7, \qquad (12)$$

so E_M / E_K is about 0.4; see the upper panel of Fig. 14. This fraction may still depend on the forcing wave number since the infrared part of the kinetic and magnetic energy spectra
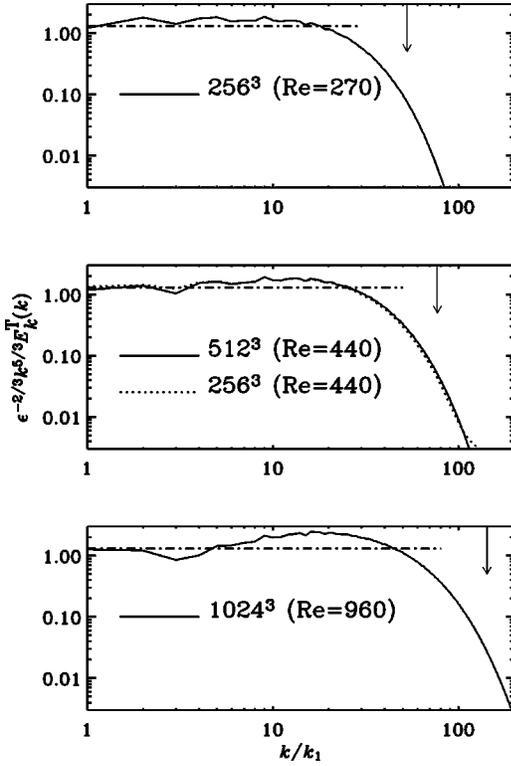
FIG. 13. Comparison of compensated three-dimensional total energy spectra for runs with magnetic Prandtl number unity but with different Reynolds numbers. In all runs the horizontal dash-dotted line represents the value 1.3. In the second panel two runs with the same Reynolds numbers, but different resolution, are compared.

FIG. 14. Relative magnetic and kinetic energies (upper panel), their respective relative dissipation rates (middle panel), and the energy dissipation rates in units of $\epsilon_0 \equiv k_1 u_{\rm rms}^3$ (last panel), as a function of Reynolds number for $\Pr_M = 1$.

can have different slopes; see Fig. 12. Naively one would just compare E_M/E_K for the three nonhelical simulations in Fig. 23, and find the ratio to decrease as the forcing wave number is increased. This is, however, not correct since all these runs have different (magnetic) Reynolds numbers. A more comprehensive study, where the Reynolds number is kept constant, is therefore necessary in order to find whether or not E_M/E_K really does depend on the forcing wave number.

Equally important is the fact that also the energy dissipation rates are converged for large Reynolds numbers, such that

$$\epsilon_M : \epsilon_K \approx 0.7 : 0.3, \tag{13}$$

i.e., ϵ_M exceeds ϵ_K by a factor of about 2.3; see the two lower panels of Fig. 14. The reciprocal correspondence of the ratios in Eqs. (12) and (13) is coincidental.

The fact that the dissipation rates for both magnetic and kinetic energies are asymptotically independent of Reynolds number is consistent with the basic Kolmogorov phenomenology that leads to the scale-free $k^{-5/3}$ spectrum. This result seems to exclude the possibility that in the large Reynolds number limit the magnetic energy spectrum peaks at small scales. It is worth mentioning that the ratio ϵ_M/ϵ_K depends only weakly on $\Pr_M$. In Table III we show that a 15-fold increase of the magnetic Prandtl number decreases the

energy dissipation ratio only by a factor of about 2; the data can be parametrized by the power law $\epsilon_M/\epsilon_K \approx 2.2\,\Pr_M^{-1/4}$.

About 70% of the energy that goes into the Kolmogorov cascade is eventually converted into magnetic energy by dynamo action and is then finally converted into heat via resistivity. A sketch of the energy budget is given in Fig. 15.

In the present simulations the thermal energy bath is not explicitly included, but we note that in hydromagnetic turbulence simulations with shear and rotation the resistive heat can become so important that the temperature can increase by a factor of 10; see Ref. [54].

F. Large magnetic Prandtl numbers

It has previously been argued that for $\Pr_M \gtrsim 1$ the magnetic energy spectrum is peaked at small scales [25,55,26,56]. For $\Pr_M = 1$ this claim cannot be confirmed at large Reynolds number (see Paper I). The original motivation for a peak at small scales is based on linear theory [9], which predicts a $k^{+3/2}$ spectrum; see also Sec. III B. However, the original Kazantsev model is only valid in the limit where the

TABLE III. Energy dissipation rates for four runs with different magnetic Prandtl numbers $\Pr_M$, showing that ϵ_M/ϵ_K is only weakly dependent on $\Pr_M$.

$\nu \times 10^4$	$\eta \times 10^4$	$\Pr_M$	$\epsilon_K \times 10^4$	$\epsilon_M \times 10^4$	ϵ_M/ϵ_K
1.5	4.5	0.33	0.79	2.4	3.0
1.5	1.5	1.	0.92	2.1	2.3
2.0	2.0	1.	0.87	1.9	2.2
7.5	1.5	5.	1.2	1.8	1.5
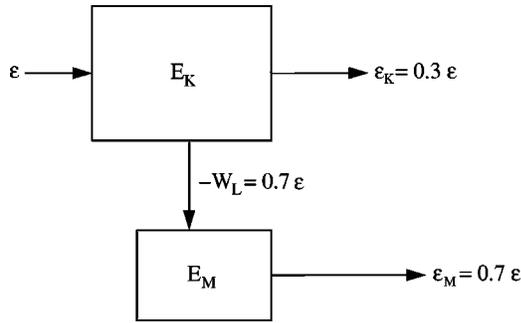
FIG. 15. Schematic view of the energy transport. Most of the energy (70%) resides in the kinetic energy reservoir, but only 30% of the total energy input is dissipated directly by viscous heating. Instead, 70% of the energy flows into the magnetic energy reservoir, and is finally dissipated by Ohmic heating.

velocity has only large scale components, which corresponds to $Pr_M \gg 1$. In order to see how our results change with varying magnetic Prandtl number we have calculated models for different values of Pr_M. One of the results is the possible emergence of a k^{-1} tail in the magnetic energy spectrum; see Fig. 16. The k^{-1} tail has recently been found in large Pr_M simulations with an imposed magnetic field [21]. The k^{-1} spectrum has its roots in early work by Batchelor [57] for a passive scalar and Moffatt [58] for the magnetic case.

In the run with $Pr_M = 30$ the viscous cutoff wave number is $k_\nu = (\epsilon_K/\nu^3)^{1/4} \approx 12$, so the k^{-1} tail is expected for wave numbers larger than that. The plot seems to suggest that the entire inertial range could have a k^{-1} spectrum, although this may well be an artifact of an insufficient inertial range. Instead, a more likely scenario is that for large hydrodynamic Reynolds numbers and large magnetic Prandtl numbers there is still a $k^{-5/3}$ range for both kinetic and magnetic energies, followed by a k^{-1} subrange for magnetic energy beyond the viscous cutoff wave number. In any case, the peak of magnetic energy would still be at small wave numbers. In summary, therefore, we find no indication of a peak of the magnetic energy spectrum at the resistive wave number.

G. Autocorrelation functions

In the context of the Zeldovich [59,60] stretch-twist-fold dynamo, the shape of the auto-correlation function of the magnetic field,
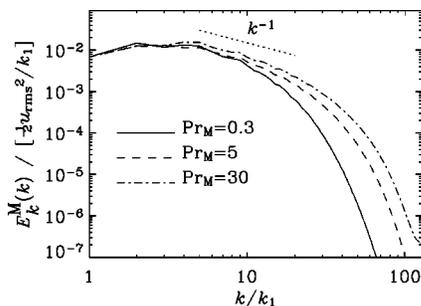
FIG. 16. Magnetic energy spectra for runs with magnetic Prandtl numbers ranging from 0.3 to 30.
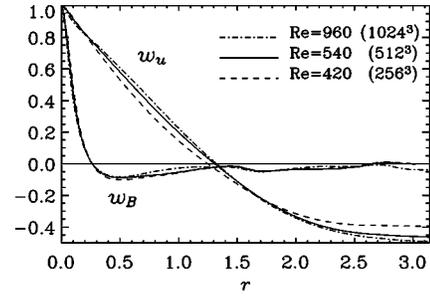
FIG. 17. Autocorrelation functions of magnetic field and velocity. Note that the autocorrelation functions are nearly independent of resolution and Reynolds number. The velocity correlation length is ~ 3 while the magnetic correlation length is ~ 0.5.

$$w_B(r) = \langle \boldsymbol{B}(\boldsymbol{x}) \cdot \boldsymbol{B}(\boldsymbol{x}+\boldsymbol{r})\rangle/\langle \boldsymbol{B}^2\rangle, \quad (14)$$

plays an important role; see also Ref. [61]. We have calculated $w_B(r)$ from the Fourier transform of the three-dimensional, time-averaged magnetic energy spectra, $E_k^M(k)$; see Fig. 17. The diffusive scale corresponds to the thickness of the narrow spike of $w_B(r)$ around the origin. The typical scale over which the magnetic field changes direction is the correlation length which corresponds to the scale where $w_B(r)$ has its minimum. We have compared $w_B(r)$ with the velocity autocorrelation function, $w_u(r)$, which is defined in an analogous manner. Note that, because of isotropy, $w_u(r)$ and $w_B(r)$ are only functions of $r = |\boldsymbol{r}|$. Similar autocorrelation functions have also been seen in simulations of convective dynamos [51]. Figure 17 shows that the velocity correlation length is ~ 3 while the magnetic field correlation length is ~ 0.5. Clearly, the magnetic correlation length is much shorter than the velocity correlation length, but it is practically independent of $Re(=Re_M)$ and certainly much longer than the resistive scale, $\sim 2\pi/k_d \approx 0.04$.

H. Structure functions

In numerical turbulence the signed structure functions for odd moments are usually not well converged. It is therefore customary to use unsigned structure functions, defined as

$$S_p(l) = \langle |\boldsymbol{z}(x+l) - \boldsymbol{z}(x)|^p\rangle, \quad (15)$$

where $\boldsymbol{z}(x)$ is one of the two Elsasser variables

$$\boldsymbol{z}^\pm = \boldsymbol{u} \pm \boldsymbol{B}/\sqrt{\rho\mu}. \quad (16)$$

The structure function exponents $S_p(l)$ normally show a power-law scaling

$$S_p(l) \propto l^{\zeta_p}, \quad (17)$$

where ζ_p is the pth order structure function scaling exponent. Here, because of isotropy, we usually consider the dependence on one spatial coordinate, x, but we also discuss the more general case below.

In Paper I we have shown that $\zeta_3 \approx 1.0$ and $\zeta_4 \approx 1.3$. This is our strongest evidence that the asymptotic inertial range scaling is $k^{-5/3}$ and that the $k^{-3/2}$ scaling seen in the upper panel of Fig. 7 is due to the bottleneck effect [44]. True
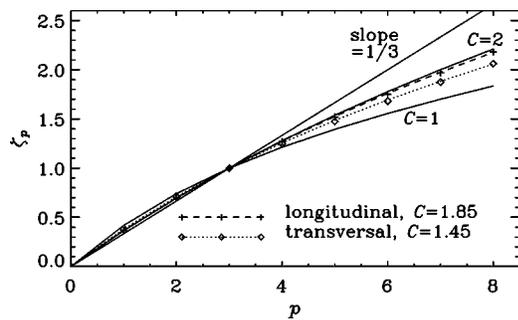
FIG. 18. Longitudinal and transversal structure function exponents for the Elsasser variables for run D.

FIG. 19. Longitudinal structure function exponents for the Elsasser variables, compared with those for velocity and magnetic field separately for run D.

Iroshnikov-Kraichnan scaling would imply $\zeta_4 = 1$, whereas $\zeta_3 = 1$ is consistent with Goldreich-Sridhar scaling.

We find that the second-order scaling exponent is $\zeta_2 = 0.7$, which again indicates that the inertial range has a slope $k^{-\zeta_2-1} \approx k^{-5/3}$, in support of our findings from the one-dimensional energy spectra. Making use of the extended self-similarity hypothesis [62] we find that for all p, the values of ζ_p are consistent with the generalized She-Leveque formula [63]

$$\zeta_p = \frac{p}{9} + C \left[1 - \left(1 - \frac{2/3}{C} \right)^{p/3} \right], \qquad (18)$$

where C is interpreted as the codimension of the dissipative structures. We find that $C = 2$ (corresponding to one-dimensional, tubelike dissipative structures) gives a reasonable fit to the longitudinal structure function exponents; see Fig. 18. If we allow for fractal codimensions, then $C = 1.85$ gives the best fit for the longitudinal structure function exponents and $C = 1.45$ for the transversal ones.

A similar difference between transversal and longitudinal structure functions has previously been found [46,64]. It has been argued [64] that this difference is an artifact of the forcing being in the same direction as the direction in which the structure functions are calculated. In our simulation, however, the forcing is chosen randomly in an isotropic manner. In addition, we have also performed a calculation were we average structure functions calculated in 91 different directions distributed isotropically over the unit sphere. In this calculation we find again the same difference between longitudinal and transversal structure functions. Additional support to this result comes from the fact that longitudinal one-dimensional energy spectra are slightly steeper than the transversal ones. A possible explanation for the difference between longitudinal and transversal structure functions has been offered by Siefert and Peinke [69], who find different cascade times for longitudinal and transversal spectra.

As stated above, our results for the longitudinal structure functions of the Elsasser variables follow the generalized She-Leveque formula with codimension $C = 2$ quite well. It is difficult to make precise comparisons with earlier work where often somewhat different cases are considered. The perhaps closest comparison is possible with the transonic hydromagnetic turbulence simulations of Padoan *et al.* [65]. They consider only velocity structure functions, but since
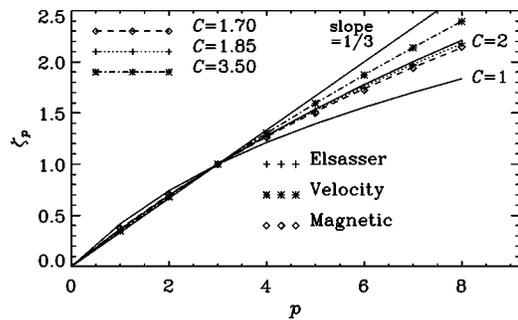
they have a weak magnetic field, the velocity is similar to the Elsasser variables. They find that for small Mach numbers the structure function scaling has codimension $C \approx 2$, while for supersonic turbulence they find $C \approx 1$. For increasing Mach numbers they see a continuous decrease from $C = 2$ to $C = 1$. This is consistent with our result of $C = 1.85$ since we have a small but finite Mach number, and would therefore expect a somewhat smaller value than $C = 2$, but considerably larger than $C = 1$.

In another set of forced turbulence simulations, Cho *et al.* [33] find that the velocity structure function has again codimension $C = 2$. We emphasize that in Ref. [33] the structure functions are calculated perpendicular to the local magnetic field, and not along the global coordinate axis. In addition, they look at velocity scaling while we concentrate on Elsasser variables. Their results can therefore not straightforwardly be compared with ours, and the similarity is probably accidental. Indeed, it is shown in Ref. [66] that structure functions calculated perpendicular to the local magnetic field and those calculated along the global coordinate axis are *not* comparable.

On the other hand, in simulations of decaying magnetohydrodynamic (MHD) turbulence at a resolution up to 512^3 collocation points, Biskamp and Müller [17] found the codimension of the Elsasser variables to be $C = 1$. At first glance this seems to contradict our results, but the fact that they have considered decaying turbulence, and that the magnetic field is decaying more slowly than the kinetic energy, implies that they have a much stronger magnetic field relative to kinetic field than we do. Furthermore, we find (see Fig. 19) that the magnetic field is much more intermittent than the velocity field [66]. It is therefore not surprising that they find different intermittency in their decay simulation than we do in our forced simulation.

Next we look at the longitudinal structure function scaling exponents for magnetic field and velocity, as well as for the Elsasser variables; see Fig. 19. The velocity is known to be generally less intermittent than the magnetic field [66]. While the Elsasser variables follow the standard She-Leveque scaling ($C = 2$) rather well, the velocity is less intermittent ($C = 3.5$) and the magnetic field is more intermittent ($C = 1.7$). Obviously, a codimension larger than the embedding dimension does not have a direct geometrical meaning, so the value of C for the velocity should not be interpreted as
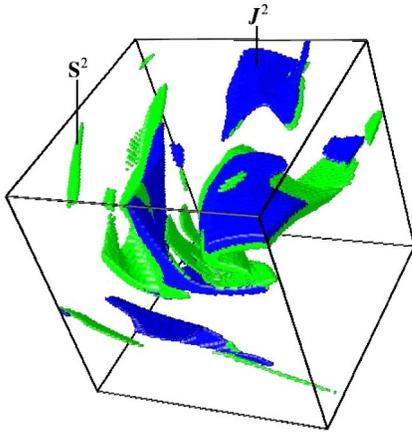
FIG. 20. Contours of J^2 (blue or dark gray) and $\mathbf{S}^2$ (green or light gray) showing the dissipative structures of magnetic and kinetic energy, respectively. Only a very small subvolume $(1/16^3)$ of the entire simulation domain of run E is shown.

FIG. 21. Contours of B^2 (blue or dark gray) and $\boldsymbol{\omega}^2$ (green or light gray) for the same small subvolume as shown in Fig. 20. Note that the areas with strong B^2 are more extended than those with strong J^2 (cf. Fig. 20) and that the locations of high $\boldsymbol{\omega}^2$ and high $\mathbf{S}^2$ are near to each other, but otherwise different in their detailed appearance (see Fig. 20), even though $\langle\boldsymbol{\omega}^2\rangle=\langle 2\mathbf{S}^2\rangle$.

a codimension, but just as an indicator for a low degree of intermittency.

I. Visualizations

In view of the discussion on the dimensionality of the dissipative structures in hydromagnetic turbulence, it is desirable to obtain an estimate simply by visual inspection. In Fig. 20 we show, for a small subvolume of the entire simulation domain, surfaces of constant J^2 (Joule dissipation) and $\mathbf{S}^2$ (viscous dissipation). Generally, the approximate dimensionality of both dissipative structures is somewhere between sheets and tubes, although J^2 appears to be perhaps slightly more sheetlike. We conclude that the dimensionality of J^2 is consistent with what one would have expected from the estimate $C=1.7$ obtained in the preceding subsection. For the dissipative structures of kinetic energy, on the other hand, the estimate $C=3.5$ exceeded the embedding dimension and did therefore not make geometrical sense anyway. The qualitative inspection of $\mathbf{S}^2$ would have suggested a codimension between 1 and 2. We therefore conclude that C can only be regarded as a fit parameters and that there is not always an obvious connection with the actual appearance of the dissipative structures.

It should be noted that normally when one talks about structures in turbulence one often talks about vortex tubes and, in the magnetic case, magnetic flux tubes. These are quite distinct from the dissipative structures. Vorticity $\boldsymbol{\omega}=\boldsymbol{\nabla}\times\boldsymbol{u}$ and rate of strain tensor $\mathbf{S}$ characterize, respectively, the antisymmetric and symmetric parts of the velocity gradient matrix, and are therefore not expected to look similar. On the other hand, $\langle\boldsymbol{\omega}^2\rangle=\langle 2\mathbf{S}^2\rangle$, where and angular brackets denote volume averages, and Fig. 21 shows that both $\boldsymbol{\omega}^2$ and $\mathbf{S}^2$ exhibit similar length scales. The difference is more pronounced in the magnetic case, where J is clearly dominated by smaller scale structures while B can exhibit structures of much larger scale. This is shown in Fig. 22 where we visualize magnetic field vectors in the full box at those locations where the field exceeds three times the rms value. The strong

field turns out to be of surprisingly large scale, even though this dynamo has no helicity and no large scale field in the usual sense; cf. Ref. [5]. The large scale structures we find are reminiscent of the ropes discussed in Refs. [60,61], although they seem to be more sheetlike [67], and their thickness is of the order of the resistive scale [68].

V. CONNECTION WITH HELICAL TURBULENCE

Finally we comment on some differences between helical and nonhelical turbulence. In the case of helical forcing one
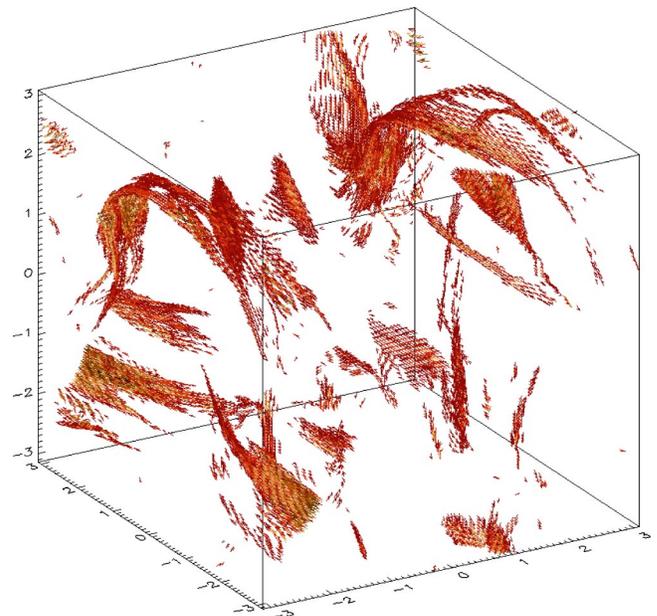
FIG. 22. Magnetic field vectors of run E shown at those locations where $|B\rangle>3B_{\mathrm{rms}}$. Note the long but thin arcadelike structures extending over almost the full domain. The structures are sheetlike with a thickness comparable to the resistive scale.
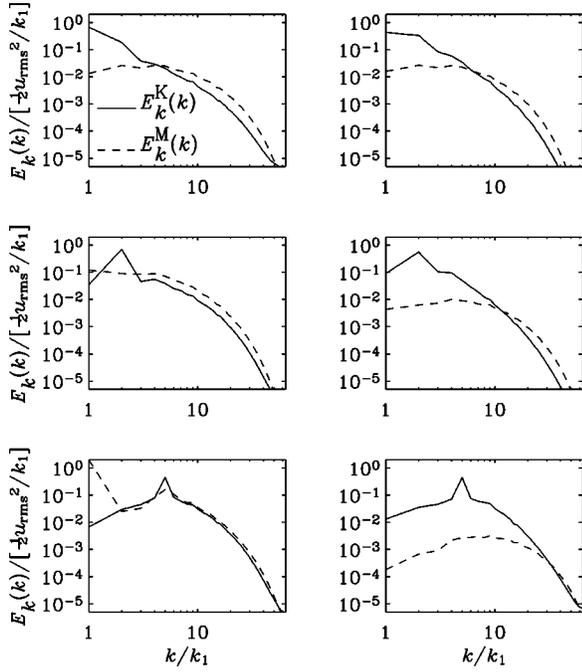
FIG. 23. Three-dimensional kinetic and magnetic energy spectra, normalized by $\frac{1}{2}u_{rms}^2/k_1$, for runs with and without helicity (left and right hand columns, respectively) and for the different forcing wave numbers: $k_f = 1.5$ (top), 2.3 (middle), 5.1 (bottom). 128^3 mesh points.

expects an *inverse* cascade to smaller wave numbers, rather than a direct cascade to larger wave numbers. We can now identify two reasons why this has not really been seen in early turbulence simulations with helical forcing [23]. On the one hand, the inverse cascade takes a resistive time to develop [5], and this time tends to be too long if magnetic hyperdiffusivity is used [28]. In Ref. [23] magnetic hyperdiffusivity was indeed used and the resistive time was at least a hundred times longer than the duration of the runs, so no inverse cascade should be expected. But there is another more important reason. In order for the inverse cascade to develop, one has to have some scale separation, i.e., the magnetic field must be allowed to grow on scales larger than the forcing scale (which corresponds to the energy carrying scale) of the turbulence. This was not the case in the early simulations and may explain why the inverse cascade has not been seen in Ref. [23] and that those results should therefore be closer to the case without helicity. To substantiate this, we have carried out simulations with helical and nonhelical forcing using the modified forcing function

$$f_k = \mathbf{R} \cdot f_k^{(\text{nohel})} \quad \text{with} \quad \mathbf{R}_{ij} = \frac{\delta_{ij} - i\sigma\epsilon_{ijk}\hat{k}_k}{\sqrt{1+\sigma^2}}, \quad (19)$$

where $f_k^{(\text{nohel})}$ is the nonhelical forcing function of Eq. (7). In the helical case ($\sigma = \pm 1$) we recover the forcing function used in Ref. [5], and in the nonhelical case ($\sigma = 0$) this forcing function becomes equivalent to that of Eq. (7).

We show in Fig. 23 the energy spectra of helical and nonhelical simulations with forcing at wave number $k_f = 1.5$ (no scale separation), $k_f = 2.3$ (weak scale separation), and $k_f = 5$ (considerable scale separation). For $k_f = 1.5$ the spectra of the helical and nonhelical simulations are indeed quite similar to each other (e.g., no inverse cascade and slight superequipartition at $k > 5$). For $k_f = 5.1$, on the other hand, the spectra are quite different and there is no inverse cascade in the nonhelical case.

VI. CONCLUSIONS

In the present paper we have studied nonhelical MHD turbulence without imposed large scale fields. We find that, in order to get dynamo action, the magnetic Reynolds number has to exceed the critical value $\text{Re}_M^{(\text{crit})} \approx 30$. When the dynamo is in the kinematic regime (the magnetic field is still too weak to affect the velocity) we see a kinetic energy spectrum with the Kolmogorov $k^{-5/3}$ inertial range, while the magnetic energy spectrum shows the expected $k^{3/2}$ Kazantsev slope (*increasing* with k).

As the dynamo gets saturated we find that there is a short inertial range where the magnetic and kinetic energy spectra are parallel. This is only seen in the largest of our simulations with 1024^3 mesh points. The magnetic energy spectrum exceeds the kinetic energy spectrum by a factor of ≈ 2.5, which seems to be more or less the asymptotic value as Re grows larger. At first glance one is led to believe that the saturated energy spectra exhibit a $k^{-3/2}$ inertial range, but we argue that this is due to a strong bottleneck effect. For one-dimensional spectra the bottleneck effect becomes much weaker and they have the expected $k^{-5/3}$ slope. We have demonstrated that simulations without magnetic fields show the same bottleneck effect. Also the second-order structure functions are consistent with a $k^{-5/3}$ scaling. We therefore conjecture that for larger values of Re one will see a $k^{-5/3}$ subrange also for the three-dimensional MHD spectra, although the bottleneck effect will continue to affect at least one decade or more in wave numbers just before the dissipative subrange.

At large scales ($1 \leq k \leq 5$) we see a $k^{1/3}$ behavior of the magnetic field. However, if we force the flow at $k_f \gg k_1$ (i.e., the energy is being injected at scales much smaller than the box size), we find that for $k \ll k_f$ the kinetic and magnetic energy spectra scale almost like k^2, although the kinetic energy spectrum is somewhat shallower which may be an artifact of the finite size of the computational domain.

Concerning the structure functions we find that our simulations are in good agreement with those found by Padoan *et al.* [65]. The Elsasser variables follow the She-Leveque scaling with a codimension somewhat less than 2, which is what one would expect since our simulation is weakly compressible. We also find that the magnetic field is more intermittent than the velocity, which is qualitatively consistent with earlier findings [10]. Quantitatively, in terms of structure function exponents, this has recently also been found by Cho

et al. [66], but it is still not known what is the cause of this difference between the intermittency of magnetic and kinetic fields.

In the case of magnetic Prandtl numbers larger than unity, there are indications of a k^{-1} range for the magnetic energy spectrum below the viscous cutoff wave number. In order to ensure that this is really the asymptotic slope, yet larger simulations are required.

[1] G. K. Batchelor, Proc. R. Soc. London, Ser. A **201**, 405 (1950).

[2] L. Biermann and A. Schlüter, Phys. Rev. **82**, 863 (1951).

[3] M. Steenbeck, F. Krause, and K.-H. Rädler, Z. Naturforsch. A **21A**, 369 (1966).

[4] A. Pouquet, U. Frisch, and J. Léorat, J. Fluid Mech. **77**, 321 (1976).

[5] A. Brandenburg, Astrophys. J. **550**, 824 (2001).

[6] M. L. Goldstein, D. A. Roberts, and C. A. Fitch, J. Geophys. Res., [Atmos.] **99**, 11519 (1994).

[7] K. Roettiger, J. M. Stone, and J. O. Burns, Astrophys. J. **518**, 594 (1999).

[8] R. M. Kulsrud, R. Cen, J. P. Ostriker, and D. Ryu, Astrophys. J. **480**, 481 (1997).

[9] A. P. Kazantsev, Zh. Eksp. Teor. Fiz. **53**, 1806 (1967) [Sov. Phys. JETP **26**, 1031 (1968)].

[10] M. Meneguzzi, U. Frisch, and A. Pouquet, Phys. Rev. Lett. **47**, 1060 (1981).

[11] N. L. Peffley, A. B. Cawthorne, and D. P. Lathrop, Phys. Rev. E **61**, 5287 (2000).

[12] C. B. Forest, R. A. Bayliss, R. D. Kendrick, M. D. Nornberg, R. O'Donnell, and E. J. Spence, Magnetohydrodynamics **38**, 107 (2002).

[13] D. R. Sisan, W. L. Shew, andD. P. Lathrop, Phys. Earth Planet. Inter. **135**, 137 (2003).

[14] P. Goldreich and S. Sridhar, Astrophys. J. **438**, 763 (1995).

[15] R. S. Iroshnikov, Astron. J. SSSR **40**, 742 (1963) [Sov. Astron. **7**, 566 (1963)]; R. H. Kraichnan, Phys. Fluids **8**, 1385 (1965).

[16] J. Cho and E. T. Vishniac, Astrophys. J. **539**, 273 (2000).

[17] D. Biskamp and W.-C. Müller, Phys. Plasmas **7**, 4889 (2000).

[18] J. Maron and P. Goldreich, Astrophys. J. **554**, 1175 (2001).

[19] D. Balsara and A. Pouquet, Phys. Plasmas **6**, 89 (1999).

[20] N. E. L. Haugen and A. Brandenburg, e-print astro-ph/0402281.

[21] J. Cho, A. Lazarian, and E. T. Vishniac, Astrophys. J. **566**, L49 (2002).

[22] R. M. Kulsrud and S. W. Anderson, Astrophys. J. **396**, 606 (1992).

[23] S. Kida, S. Yanase, and J. Mizushima, Phys. Fluids A **3**, 457 (1991).

[24] H. Chou, Astrophys. J. **556**, 1038 (2001).

[25] J. Maron and S. C. Cowley, e-print astro-ph/0111008.

[26] A. A. Schekochihin, S. C. Cowley, G. W. Hammett, J. L. Maron, and J. C. McWilliams, New J. Phys. **4**, 84 (2002).

[27] G. Falkovich, Phys. Fluids **6**, 1411 (1994).

[28] A. Brandenburg and G. R. Sarson, Phys. Rev. Lett. **88**, 055003 (2002).

[29] L. J. Milano, W. H. Matthaeus, P. Dmitruk, and D. C. Montgomery, Phys. Plasmas **8**, 2673 (2001).

[30] S. Oughton, W. H. Matthaeus, and S. Ghosh, Phys. Plasmas **5**, 4235 (1998).

[31] J. Cho and A. Lazarian, Mon. Not. R. Astron. Soc. **345**, 325 (2003).

[32] M. M. Mac Low, R. S. Klessen, and A. Burkert, Phys. Rev. Lett. **80**, 2754 (1998).

[33] J. Cho, A. Lazarian, and E. T. Vishniac, Astrophys. J. **564**, 291 (2002).

[34] S. Boldyrev, Å. Nordlund, and P. Padoan, Astrophys. J. **573**, 678 (2002).

[35] N. E. L. Haugen, A. Brandenburg, and W. Dobler, Astrophys. J. **597**, L141 (2003) (Paper I).

[36] The Pencil Code is a high-order finite-difference code (sixth order in space and third order in time) for solving the compressible MHD equations; http://www.nordita.dk/data/brandenb/pencil-code

[37] J. H. Williamson, J. Comput. Phys. **35**, 48 (1980).

[38] J. Léorat, A. Pouquet, and U. Frisch, J. Fluid Mech. **104**, 419 (1981).

[39] A. A. Schekochihin, S. C. Cowley, J. L. Maron, and J. C. McWilliams, Phys. Rev. Lett. **92**, 054502 (2004).

[40] A. A. Schekochihin (private communication).

[41] V. G. Novikov, A. A. Ruzmaikin, and D. D. Sokoloff, Zh. Eksp. Teor. Fiz. **85**, 909 (1983) [Sov. Phys. JETP **58**, 527 (1983)].

[42] K. Subramanian, Phys. Rev. Lett. **83**, 2957 (1999).

[43] A. Schekochihin, S. Cowley, G. W. Hammett, J. L. Maron, and J. C. McWilliams, New J. Phys. **4**, 84.1 (2002).

[44] W. Dobler, N. E. L. Haugen, T. Yousef, and A. Brandenburg, Phys. Rev. E **68**, 026304 (2003).

[45] A. Vincent and M. Meneguzzi, J. Fluid Mech. **225**, 1 (1991).

[46] T. Gotoh, Comput. Phys. Commun. **147**, 530 (2002).

[47] D. H. Porter, P. R. Woodward, and A. Pouquet, Phys. Fluids **10**, 237 (1998).

[48] Y. Kaneda, T. Ishihara, M. Yokokawa, K. Itakura, and A. Uno, Phys. Fluids **15**, L21 (2003).

[49] Z.-S. She and E. Jackson, Phys. Fluids A **5**, 1526 (1993).

[50] D. Lohse and A. Müller-Groeling, Phys. Rev. Lett. **74**, 1747 (1995); D. Lohse and A. Müller-Groeling, Phys. Rev. E **54**, 395 (1996).

[51] A. Brandenburg, R. L. Jennings, Å. Nordlund, M. Rieutord, R. F. Stein, and I. Tuominen, J. Fluid Mech. **306**, 325 (1996).

[52] A. Brandenburg, W. Dobler, and K. Subramanian, Astron. Nachr. **323**, 99 (2002).

[53] M. Lesieur, *Turbulence in Fluids* (Martinius Nijhoff, Dor-

drecht, 1990).

[54] A. Brandenburg, Å. Nordlund, R. F. Stein, and I. Torkelsson, Astrophys. J. **458**, L45 (1996).

[55] J. Maron and E. G. Blackman, Astrophys. J. **566**, L41 (2002).

[56] A. A. Schekochihin, J. L. Maron, S. C. Cowley, and J. C. McWilliams, Astrophys. J. **576**, 806 (2002).

[57] G. K. Batchelor, J. Fluid Mech. **5**, 113 (1959).

[58] H. K. Moffatt, J. Fluid Mech. **17**, 225 (1963).

[59] Ya. B. Zeldovich, A. A. Ruzmaikin, and D. D. Sokoloff, *Magnetic Fields in Astrophysics* (Gordon and Breach, New York, 1983).

[60] Ya. B. Zeldovich, A. A. Ruzmaikin, and D. D. Sokoloff, *The Almighty Chance* (World Scientific, Singapore, 1990).

[61] K. Subramanian, Mon. Not. R. Astron. Soc. **294**, 718 (1998).

[62] R. Benzi, S. Ciliberto, R. Tripiccione, C. Baudet, F. Massaioli, and S. Succi, Phys. Rev. E **48**, R29 (1993).

[63] Z.-S. She and E. Leveque, Phys. Rev. Lett. **72**, 336 (1994).

[64] D. Porter, A. Pouquet, and P. Woodward, Phys. Rev. E **67**, 026301 (2002).

[65] P. Padoan, R. Jimenez, Å. Nordlund, and S. Boldyrev, Phys. Rev. Lett. **92**, 191102 (1994).

[66] J. Cho, A. Lazarian, and E. T. Vishniac, Astrophys. J. **595**, 812 (2003).

[67] H. Politano, A. Pouquet, and P. L. Sulem, Phys. Plasmas **8**, 2931 (1995).

[68] A. Brandenburg, I. Procaccia, and D. Segel, Phys. Plasmas **2**, 1148 (1995).

[69] M. Siefert and J. Peinke, e-print physics/0309106.